ACS OMEGA

Open Access

http://pubs.acs.org/journal/acsodf

Article

V_2O_5–Fe_3O_4/rGO Ternary Nanocomposite with Dual Applications as a Dye Degradation Photocatalyst and OER Electrocatalyst

Fatemeh Jafari and Fatemeh Rahnemaye Rahsepar*

Cite This: *ACS Omega* 2023, 8, 35427−35439

Read Online

ACCESS | Metrics & More | Article Recommendations | Supporting Information

ABSTRACT: The design and synthesis of structured nanomaterials with dual properties have always been highly attractive in various fields, especially in the reduction of environmental pollution as well as the generation of renewable energy. In this study, the synthesized ternary V_2O_5–Fe_3O_4/rGO nanocomposite was investigated to evaluate both the photocatalytic and electrocatalytic activities for the removal of methylene blue (MB) dye under UV/visible light radiation and oxygen evolution reaction (OER), respectively. The magnetized V_2O_5–Fe_3O_4/rGO nanocomposite is characterized by TEM, FE-SEM (with coupling by elemental mapping), EDS, XRD, FTIR, Raman, PL, DRS, and UV–vis analyses. The obtained results show that the graphene oxide substrate is decorated very well using Fe_3O_4 and V_2O_5 nanoparticles and converted to reduced graphene oxide (rGO). Furthermore, the V_2O_5–Fe_3O_4/rGO nanocomposite is considered as an active catalyst material to modify the commercial glassy carbon electrode for OER using linear sweep voltammetry (LSV). The photocatalytic activity of this novel nanocomposite revealed 89.2% (k_{obs} = 1.7 × 10^{-2} min^{-1}) and 76% (k_{obs} = 8.3 × 10^{-3} min^{-1}) degradation efficiencies of MB dye under UV and visible light irradiation at room temperature, respectively, and the surface area of the V_2O_5–Fe_3O_4/rGO nanocomposite was examined to be 705.8 cm^2/g by N_2 adsorption–desorption isotherms. In addition, electrochemical measurements determined the best OER performance of the ternary nanocomposite with the lowest overpotential (458 mV) and Tafel slope (132 mV dec^{-1}) compared to the rGO substrate, Fe_3O_4, V_2O_5 nanoparticles, and binary nanocomposites. This work shows much enhancements in both photocatalytic and electrocatalytic activities due to the synergistic effect of the decorated GO support with V_2O_5 and Fe_3O_4 nanoparticles.

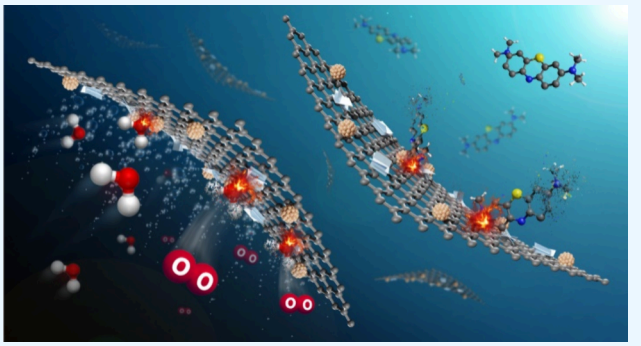

1. INTRODUCTION

Recently, controlled synthesis for the design of 2D multicomponent nanomaterials has drawn a great deal of recent attention because of enhancing their efficiency for desired applications compared with single-component nanomaterials.[1] When designed multipart materials can exhibit dual applications, they will certainly become a more critical issue for further consideration. On the other hand, the design and synthesis of multicomponent nanocatalysts that are effective in both photovoltaic and electrochemical fields have always been of interest to researchers due to environmental issues.[2]

In the past few years, the negative impact of certain industrial wastes, particularly dye effluent, on human lives is a significant contemporary issue, especially with respect to water pollution.[3] Various synthesized heterogeneous catalysts have been extensively researched to remove pollutants from industrial wastewater.[4,5] Due to the economic and environment-friendly properties, photocatalytic degradation technology is considered as a promising application for organic wastewater treatment in which organic pollution molecules are broken down into H_2O, CO_2, Cl, and so on.[6,7] In the topic of catalysts, whether photocatalysts or electrocatalysts, the support of catalysts plays a crucial role in catalytic activities, especially with synergistic effects, for the desired applications.[8,9]

In recent decades, graphene has garnered much attention among all carbon materials because of the outstanding properties it possesses, such as an expansive surface area,[10] outstanding charge carrier mobility,[11] excellent electrical conductivity at room temperature,[12] high thermal conductivity,[13] strong carrier density,[14] suitable optical transmittance,[12] and chemical stability,[15] in addition to its potential applications in water purification as a supporting template. Graphene oxide (GO) and reduced graphene oxide (rGO) have been modified with various functional groups containing carboxyl, epoxy,

Received: August 17, 2023
Accepted: September 1, 2023
Published: September 13, 2023

carbonyl, and hydroxyl groups to make them less aggregating and more dispersing in an aqueous solution.[16]

Furthermore, the novel hybrid nanocomposites including metal oxide nanoparticles and GO/rGO support offer a remarkable potential to enhance the photocatalytic activity because of a broad range of various physical, chemical, and mechanical properties.[17] Among several metal oxides used to prepare hybrid nanocomposites, vanadium pentoxide (V_2O_5) with a band gap of 2.2 eV has attracted notable interest because of its inimitable properties like excellent chemical and thermal stabilities and structure for photocatalytic degradation applications.[18−21] In one of the most recent studies to remove MB dye by using vanadium pentoxide, V_2O_5 nanorods obtained from the thermal decomposition of ammonium metavanadate have shown photocatalytic efficiency of 92.4% at 40 °C under visible light,[22] However, V_2O_5 nanoparticles synthesized by the flame spray pyrolysis process revealed only about 81% MB dye degradation.[23] Furthermore, the heterojunction of 2D hybrid ZnO/V_2O_5 has enhanced the efficiency to remove MB dye to 90% compared to pristine zinc oxide under visible light irradiation.[24] Also, another heterojunction structure of V_2O_5 and $BiVO_4$ has presented 92% of MB dye degradation for 180 min and an improvement in the kinetic behavior due to the increased photogenerated charge lifetime.[25]

However, photocatalytic dye degradation is limited by the low band gap energy and the combination of electrons and holes. As a result, the presence of graphene oxide nanosheets can restrict the recombination of electron−hole pairs by the highly active sites of these materials and strong $\pi-\pi$ intermolecular interactions with dyes.[26]

Another effective semiconductor is magnetite (Fe_3O_4) with 1.4 eV band gap energy and great superparamagnetic properties which are beneficial for numerous applications.[27−29] In the studies conducted using Fe_3O_4 to remove dye pollution, hybrid magnetic Fe_3O_4@SiO_2@Ru degraded 95 and 91% of methyl orange and methyl red, respectively, in acidic media,[30] and ternary Fe_3O_4/GQD/g-C_3N_4 heterostructure represented 100% rhodamine B (RhB) dye degradation under visible irradiation.[31] In addition, flower-like MoS_2/Fe_3O_4/rGO showed a 100% RhB degradation in 40 min under visible-light irradiation.[32]

Despite their strong magnetic properties, Fe_3O_4 nanoparticles in solution tend to cluster into big particles and decrease the dispersion; thus, rGO-based magnetic nanocomposites can inhibit the aggregation of Fe_3O_4 nanoparticles, and also an external magnetic field can be used to separate them from the solution.[33,34] Magnetically separable Fe_3O_4@rGO indicated high photocatalytic degradation of 93.3% of MB dye under visible-light degradation,[35] while the nonmagnetic Gd−V_2O_5/RGO revealed 97.12% MB dye removal under a photocatalytic degradation process.[36] In addition, in a photocatalytic investigation, V_2O_5@rGO demonstrated 98.85% degradation efficiency of MB dye,[37] while in a photoelectrocatalytic process, the same nanocomposite showed 90% photodegradation of MB dye.[38] Moreover, the magnetic $Fe_3O_4-V_2O_5$/rGO nanocomposite revealed effective photocatalytic degradation of Acid orange and Bismarck brown dyes.[39] Therefore, the presence of both V_2O_5 and Fe_3O_4 nanoparticles modified on rGO nanosheets can extremely limit the recombination of electron−hole pairs and enhance the degradation efficiency of nanostructures.

On the other hand, growing concerns about environmental contamination resulting from the massive consumption of nonrenewable resources such as fossil fuels have prompted the global community to investigate green and renewable energy sources. One promising approach for generating clean energy is via the electrocatalytic splitting of water using semiconductor catalysts, which has the potential to provide a sustainable source of oxygen and hydrogen.[40,41] To electrolyze water, two distinct electrochemical half-cell reactions, the oxygen evolution reaction (OER) and the hydrogen evolution reaction (HER), are required. In an electrochemical process, the reaction overpotential can be quantified by measuring the potential required to achieve a specific current density, and it is characterized as the deviation between the actual potential and the theoretical equilibrium potential for an electrode. Moreover, depending on the direction of the half-cell reaction, the overpotential could be either positive or negative. In the electrochemical water-splitting process, highly active catalysts are essential to reduce the overpotential of the OER and HER.[42] In addition, the OER/HER enables the use of non-noble metals or metal oxides as electrocatalysts in the alkaline and acidic media.[43,44] Recently, annealed V_2O_5 showed an overpotential of 514 mV at the current density of 10 mA cm^{-2}, with the Tafel slope of 147 mV dec^{-1} in 1 M KOH.[45] Polycrystalline V_2O_5 nanorods synthesized through the polymer-assisted technique coated on Ni foam represented OER properties, with the Tafel slope of 88 mV dec^{-1} and overpotential of 310 mV at 10 mA cm^{-2}.[46] Furthermore, magnetic coral-like Fe_3O_4 nanoparticles were investigated at different calcining temperatures, displaying the best performance with an overpotential of 234 mV and Tafel slope of 100 mV dec^{-1} at 450 °C.[47] In a recent theoretical study carried out on the Fe_3O_4(001) surface for OER, transition-metal atoms including Co, Cu, Ni, and Ti have been doped on the magnetic surface, and results have predicted an overpotential of about 350 mV for Co-doped Fe_3O_4 surface in alkaline solution.[48] Immobilized Fe_3O_4 nanoparticles on Ni-based MOFs (metal−organic frameworks) displayed an overpotential of 295 mV at 10 mA/cm^2 and a Tafel slope of 47.8 mV dec^{-1}.[49] Moreover, by using a coupled interface between Fe_3O_4 and CoO nanostructures on the substrate of carbon nanotubes, the overpotential and Tafel slope were obtained as 270 mV and 59 mV dec^{-1}, respectively, for OER.[50]

Since the GO or rGO sheets can significantly enhance the quantity of active sites in electrochemistry catalysts as a result of their enhanced electron transport and increased specific surface area, ths graphene-based composites modified by V_2O_5 or Fe_3O_4 nanoparticles have been investigated as excellent materials for the electrocatalytic application.[51−53] For example, $CoV_2O_6-V_2O_5$/NRGO exhibits a high intrinsic OER activity with a Tafel slope of 49.7 mV dec^{-1} at an overpotential of 300 mV.[54] Furthermore, the Fe_3O_4@Co_9S_8/rGO composite demonstrates an overpotential of 340 mV at the current density of 10 mA cm^{-2} for OER.[55] In contrast to few studies on the investigation of the electrocatalytic activity of Fe_3O_4 or V_2O_5 nanoparticles on the GO/rGO substrate, there has been no report on the $V_2O_5-Fe_3O_4$/rGO nanocomposite for the OER. Thus, the dual applications of the ternary $V_2O_5-Fe_3O_4$/rGO nanocomposite as a photocatalyst for MB degradation and an electrocatalyst for oxygen evolution reaction have been investigated for the first time in this research.

https://doi.org/10.1021/acsomega.3c06094
ACS Omega 2023, 8, 35427−35439

2. EXPERIMENTAL DETAILS

2.1. Materials. Graphite powder (size <150 μm, 99.99%), hydrochloric acid (HCl 37%), hydrogen peroxide (H_2O_2 20%), potassium persulfate ($K_2S_2O_8$), potassium permanganate ($KMnO_4$), sodium nitrate ($NaNO_3$), sulfuric acid (H_2SO_4 95−97%), phosphorus pentoxide (P_2O_5), ethylene glycol ($C_2H_6O_2$), iron(III) chloride ($FeCl_3.6H_2O$), sodium acetate ($C_2H_3NaO_2$), trisodium citrate ($Na_3C_6H_5O_7$), ammonium metavanadate (NH_4VO_3), absolute ethanol (C_2H_5OH 99%), and ammonia solution 25% (NH_3, Merck) were procured from Merck Co.

2.2. Synthesis of GO, rGO, and V_2O_5@rGO. The modified Hummer's technique was used to synthesize GO;[56] briefly, the graphite powder was first mixed with an 80 °C solution of P_2O_5, $K_2S_2O_8$, and H_2SO_4 in a pretreatment step, and then the dark blue mixture was washed and filtered to achieve the neutral pH. The prepared preoxidized graphite powder was poured into a cold 0 °C solution of H_2SO_4 and $NaNO_3$, and then $KMnO_4$ was gradually added within 20 min under stirring and cooling. The obtained solution was stirred for 60 min at 35 °C, which turned to a light brownish pasty mixture. The solution is mixed with DI water under the temperature of 98 °C for 30 min and oxidized with H_2O_2 to achieve a bright yellow solution. The mixture was washed with DI water and 10% HCl solution, centrifuged, and dried at 65 °C for 5 h to reach the reddish brown graphene oxide nanosheets. Then, the synthesized graphene oxide was converted to reduced graphene oxide using a chemical reduction process with ethylene glycol. In the next step, a standard solvothermal technique was used to prepare the V_2O_5@rGO nanocomposites. First, 500 mg of NH_4VO_3 was added to heated ethylene glycol, and the mixture was stirred for 4 h. The GO dispersion containing 30 mg of synthesized GO powder in 50 mL of ethylene glycol was added to the prepared NH_4VO_3 solution and was further stirred for 6 h. The resulting solution was later transferred into a stainless steel autoclave with Teflon lining and kept for 24 h at 180 °C. The solution was dried in the oven at 70 °C and annealed at 500 °C for 2 h. The same procedure was used to produce V_2O_5 without graphite oxide powder.[57]

2.3. Synthesis of Fe_3O_4 and Fe_3O_4@rGO. By using a one-pot solvothermal process, the Fe_3O_4@rGO nanocomposite was prepared. 50 mg of the synthesized GO and 500 mg of $FeCl_3.6H_2O$ were dissolved in 25 mL of ethylene glycol and stirred for 2 h, followed by 25 mg of $Na_3C_6H_5O_7$ and 1.8 g NaOAc. To make a clear mixture, the solution was ultrasonicated continuously for 30 min. Then, the mixture was sealed in a Teflon-lined autoclave at 200 °C for 16 h. The black Fe_3O_4@rGO nanocomposites were centrifuged and carefully washed with ethanol/deionized water for purification. The Fe_3O_4 nanoparticles were made using the same processes as the above without the use of GO powder.[58]

2.4. Synthesis of V_2O_5−Fe_3O_4/rGO. The ternary V_2O_5−Fe_3O_4/rGO nanocomposite was fabricated using 100 mg of the synthesized Fe_3O_4@rGO powder, which was dissolved in 50 mL of ethylene glycol and stirred for 3 h. Then, the pH was adjusted with ammonia solution (25%) to 11−12, and the solution was mixed for 2 h. After 500 mg of NH_4VO_3 was added, the solution was stirred for 8 h at 70 °C and then transferred to a Teflon-lined autoclave for 48 h at 180 °C. Then, the resultant combination was washed, dried, and annealed for 2 h at 500 °C, yielding the brownish yellow V_2O_5−Fe_3O_4/rGO sample.

2.5. Characterization Techniques. Fourier transform infrared spectroscopy (FTIR) (Thermo AVATAR) and XRD analysis (Philips PW-1730) were conducted to analyze the functional groups and crystalline structures of the synthesized samples, respectively. Also, Raman spectroscopy was run to consider the vibrational modes in the ternary nanocomposite. Field emission scanning electron microscopy (FE-SEM) coupled with elemental mapping and energy-dispersive X-ray spectroscopy (EDS) analysis (Mira 3-XMU) and transmission electron microscopy (TEM) (Philips EM 208S) are employed to characterize the surface topography with the elemental distributions and nanoparticle morphology of the synthesized nanoparticles and also binary and ternary nanocomposites. Brunauer−Emmett−Teller (BET) (Belsorp Mini II) analysis was executed to give information about the surface areas of the ternary nanocomposite. Additionally, photoluminescence (PL) (Eclipse Agilent Technologies) and UV−visible diffuse reflectance spectroscopy (DRS) (S_4100 SCINCO) measurements were recorded to analyze the optical properties of the V_2O_5 semiconductor as the synthesized nanoparticle and the ternary nanocomposite. The electrochemical measurement was run by a PGE-18 (potentiostat/galvanostat/electrochemical impedance spectroscopy) system.

2.6. Photocatalytic Degradation Experiment. Photocatalytic investigations were conducted under the irradiation of low-pressure UV light (125 W UV lamp) and visible light (50 W LED lamp). The adsorption/desorption equilibrium was first checked by stirring 3 mg of the catalyst in a 30 mL aqueous reaction mixture (dye concentration: 9.38×10^{-6} M at pH = 7) in the dark for 30 min. Then, 2 mL of the reaction mixture was taken out at periodic intervals throughout the irradiation period. An external magnet was used to separate the photocatalyst, and the supernatant was then gathered. UV−visible spectrophotometry at a fixed wavelength of 664 nm for the MB dye was utilized to assess the residual dye concentration in the solution. The following equation (eq 1) was used to determine the photocatalytic degradation of nanostructures.

$$\text{Degradation efficiency}(\%) = [1 - C_t/C_o] \times 100 \quad (1)$$

In the above equation, C_o and C_t represent the original dye concentration and the amount of dye that is still present in the mixture at time t, respectively. The pH of the solution containing MB dye was tested by employing either a 0.1 M HCl or a NaOH solution during a series of experiments. In 30 mL of the solution, 3 mg of the ternary photocatalyst was added, and the initial and final pH values of the solution were recorded. Moreover, after one cycle of degradation, the nanocomposite was separated by a magnetic field, washed with water/ethanol, and dried in an oven for the recycling experiment.

2.7. Preparation of Modified Glassy Carbon Electrode (GCE) and Electrochemical Measurement. A homogeneous solution made of 2 mg of synthesized samples, 10 vol % nafion (0.2 wt %), and 800 μL of ethanol was first sonicated for 30 min. After sonication, 6 μL of the suspension was drop-casted evenly on a cleaned glassy carbon electrode (GCE), which was utilized as the working electrode, and subsequently immersed in an electrolyte of 1 M KOH. The counter and reference electrodes were considered to be Pt and silver chloride, respectively (Ag/AgCl). Linear sweep voltammetry

https://doi.org/10.1021/acsomega.3c06094
ACS Omega 2023, 8, 35427−35439

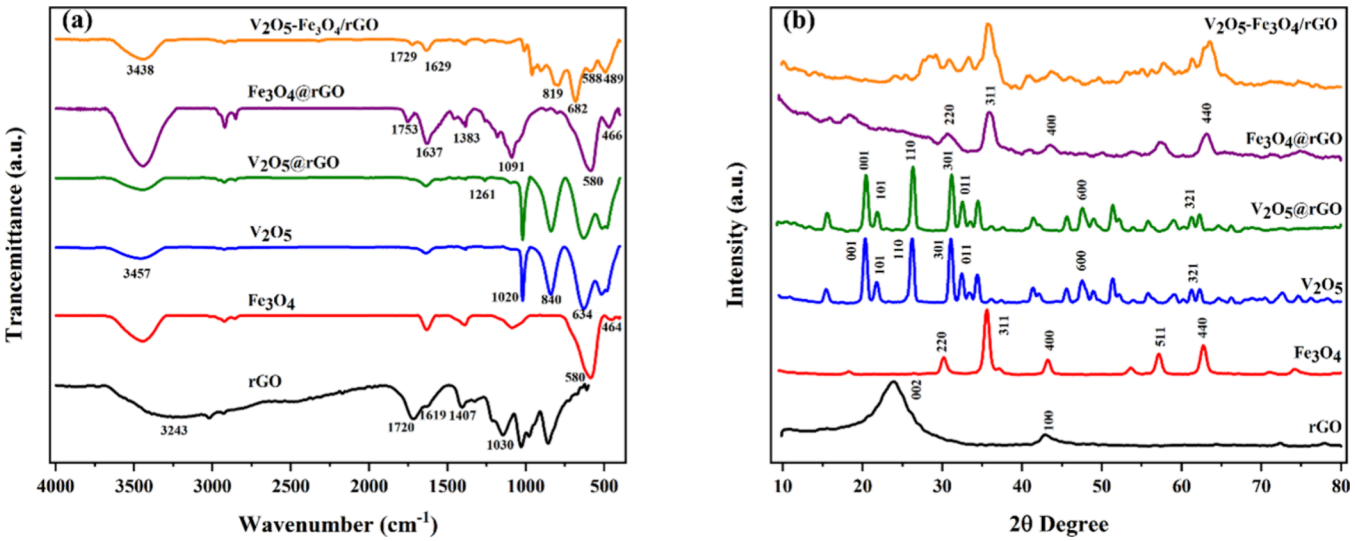

Figure 1. (a) FT-IR spectra and (b) XRD patterns of GO (rGO), Fe_3O_4, V_2O_5, V_2O_5@rGO, Fe_3O_4@rGO, and V_2O_5−Fe_3O_4/rGO samples.

(LSV) was executed to present the electrocatalytic oxygen evolution reaction of the synthesized nanostructures. Furthermore, electrochemical impedance spectroscopy (EIS) analyses were performed over a frequency range of 0.1−1 MHz at an AC amplitude of 20 mV.

3. RESULTS AND DISCUSSION

3.1. Structural and Morphological Analysis. Figure 1a shows the FTIR analysis of GO, nanoparticles (Fe_3O_4 and V_2O_5), binary nanocomposites (V_2O_5@rGO and Fe_3O_4@rGO), and ternary nanocomposite (V_2O_5−Fe_3O_4/rGO) to consider the presence of different functional groups. The IR spectrum of functional groups on pristine GO containing oxygen demonstrates three main peaks at 3243, 1030, and 1720 cm^{-1}, attributed to the stretching vibration of the hydroxyl group, C−O (carboxyl group), and C═O (carbonyl group), respectively, while the peak at 1619 cm^{-1} can be assigned to the C═C stretch vibration in graphene skeleton rings. As shown in Figure 1a, the IR spectrum of Fe_3O_4 and V_2O_5 nanoparticles represents strong peaks at 580, 1020, and 840 cm^{-1}, which are ascribed to Fe−O, V═O, and V−O−V vibration modes, respectively. Furthermore, the roughly strong observed peak at about 3450 cm^{-1} for the nanoparticle spectra is assigned to the OH bending of water. The main peaks in the FTIR spectrum of the Fe_3O_4@rGO sample at 3438, 1637, 1091, and 1753 cm^{-1} are, respectively, related to O−H, C═C, C−O, and C═O functional groups, while the peak at 580 cm^{-1} is connected to Fe−O.[59] The presence of C═O bonds at wavenumber 1753 cm^{-1} and C═C bonds at 1637 cm^{-1} indicates the presence of rGO nanosheets. Furthermore, the IR spectrum of V_2O_5@rGO exposes all V_2O_5 vibrations, and the diffraction peak at 1261 cm^{-1} confirms the presence of rGO.[36,60] Finally, the spectrum of the ternary V_2O_5−Fe_3O_4/rGO nanocomposite shows peaks at 588, 819, and 1012 cm^{-1} related to Fe−O, V−O−V, and V═O functional groups, respectively, which confirmed the decorated GO substrate with metal oxide nanoparticles. Moreover, diffraction peaks at 1629 and 1729 cm^{-1} are attributed to the C═C and C═O stretching bonds of rGO, and a significantly reduced diffraction peak at 3438 cm^{-1} compared to the similar one in GO spectra is considered for the hydroxyl group which confirms the reduction of GO in the V_2O_5−Fe_3O_4/rGO nanocomposite.[61]

In addition, XRD patterns are employed to study the structure and interlayer distance of rGO, Fe_3O_4, V_2O_5, V_2O_5@rGO, Fe_3O_4@rGO, and V_2O_5−Fe_3O_4/rGO. The XRD pattern of rGO in Figure 1b shows a very strong peak at 2θ = 23.85°, related to the (002) crystallographic plane with an interplanar spacing of about 0.373 nm, and a weak peak at 2θ = 43° corresponded to the (100) plane of graphitic carbon. The XRD pattern of V_2O_5 nanoparticles indicates diffraction peaks at 2θ values of 20.29, 21.79, 26.19, 31.04, 32.49, 47.44, and 61.29° with crystallographic planes of (001), (101), (110), (301), (011), (600), and (321), respectively (JCPDS card no. 41-1426). Compared with the V_2O_5 diffraction pattern, the XRD pattern of V_2O_5@rGO displays all of the diffraction peaks of V_2O_5 nanoparticles at 20.5, 26.25, 31.15, 32.55, 47.5, and 61.25°. Furthermore, diffraction peaks from the (220), (311), (400), (511), and (440) crystallographic planes appeared at 2θ values of 30.17, 35.57, 43.27, 57.17, and 62.72°, respectively, in the diffraction pattern of Fe_3O_4 nanoparticles (JCPDS card no. 01-075-0449). The Fe_3O_4@rGO XRD pattern shows diffraction peaks of Fe_3O_4 nanoparticles, which confirms the correct surface modification of rGO. Finally, the XRD spectrum of V_2O_5−Fe_3O_4/rGO displays the diffraction peaks of both Fe_3O_4 and V_2O_5 nanoparticles from the crystallographic planes (110), (301), (011), (311), (321), and (440) at the corresponding 2θ values of 25.5, 31.0, 33.3, 35.75, 61.45, and 63.45°. Due to the high quantity of V_2O_5 and Fe_3O_4 nanoparticles, the diffraction peaks of rGO nanosheets disappeared, which is in agreement with EDS results.[62,63]

In addition to the aforementioned results of XRD and FTIR analyses, Raman spectroscopy is also employed to provide more complementary information about the chemical structure of the V_2O_5−Fe_3O_4/rGO ternary nanocomposite, as shown in Figure S1 (Supporting Information). The presence of D and G bands belonging to graphene oxide can be strongly observed at 1473 and 1583 cm^{-1}, respectively.[64] Furthermore, the peaks identified at wavenumbers 385, 458, and 597 cm^{-1} relate to the Fe−O vibration mode of Fe_3O_4 nanoparticles.[65] Also, the existence of two strong peaks at 525 and 693 cm^{-1} are assigned to the O−V−O bending vibration modes of V═O bending, and specific peaks at 298 and 990 cm^{-1} confirm the presence of V═O.[66]

https://doi.org/10.1021/acsomega.3c06094
ACS Omega 2023, 8, 35427−35439

For further investigation, FE-SEM, EDS, and elemental mapping analyses are employed to consider the morphology and elemental distribution of the synthesized GO substrate, Fe_3O_4, and V_2O_5 nanoparticles and binary and ternary nanocomposites. The sheetlike two-dimensional rGO with an interconnected network can provide adequate surface area for functionalization, as displayed in Figure 2a. The FE-SEM

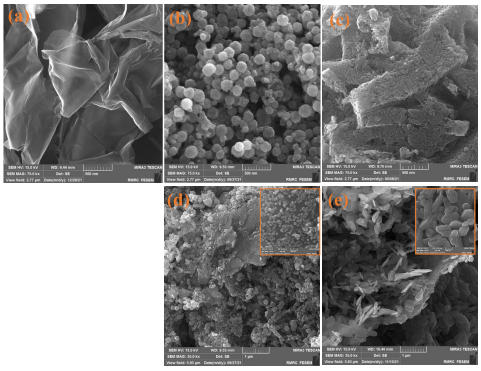

Figure 2. (a) FE-SEM images of rGO nanosheets, (b) Fe_3O_4 nanoparticles, (c) V_2O_5 nanoparticles, (d) binary Fe_3O_4@rGO, and (f) V_2O_5@rGO nanocomposites. The insets in (d) and (e) show a magnified image of binary Fe_3O_4@rGO and V_2O_5@rGO nanocomposites, respectively.

images of the synthesized Fe_3O_4 and V_2O_5 nanoparticles in Figure 2b,c, respectively, represent the nanospherical Fe_3O_4 particles and aggregated V_2O_5 nanorods as broad ribbons. Furthermore, Figure 2d and the inset display rigidly attached Fe_3O_4 nanoparticles on the rGO nanosheet surface, and elemental mapping and EDS analysis of Fe_3O_4@rGO also prove the uniform distribution of magnetic nanoparticles on rGO sheets (Supporting Information, Figure S2). A close examination of Figure 2e and the inset represents that both sides of graphene oxide sheets can be decorated by V_2O_5 nanoparticles, and elemental mapping and EDS analysis also confirm the vanadium distribution in carbon and oxygen matrix (Supporting Information, Figure S3).

Finally, the images of FE-SEM, elemental mapping, EDS analysis, and TEM of the synthesized ternary V_2O_5−Fe_3O_4/rGO nanocomposite are shown in Figure 3. Compared to Figure 2b,c, the SEM images shown in Figure 3a−c and the insets show both aggregated spherical and rod morphologies related to Fe_3O_4 and V_2O_5 particles, respectively, on graphene oxide nanosheets. Moreover, the coexistence and elemental distribution of Fe_3O_4 and V_2O_5 nanoparticles on the GO substrate were investigated using elemental mapping and EDS shown in Figure 3d−h. Both the elemental mapping and EDS results obtained indicate the suitable elemental distribution with local weight percentages of 10.6% C, 24.17% O, 39.97% V, and 25.26% Fe, which is confirmed by the XRD results. Further, TEM is used to evaluate the internal properties of the synthesized samples illustrated in Figure 3i,j. These images show the transparent rGO nanosheets in nonblack parts. Also, the agglomeration of nanoparticles on the rGO nanosheets is clear in the darker parts, and the existence of active sites on the rGO surface is represented in the nonblack regions.[67,68]

Figure 4a illustrates the UV−visible DRS of the V_2O_5 nanoparticle and V_2O_5−Fe_3O_4/rGO nanocomposite. These results are considered for the investigation of the photoconduction activity of V_2O_5 as the main semiconductor in both samples of single nanoparticles (i. e., V_2O_5) and the hybrid nanocomposite (i.e., V_2O_5−Fe_3O_4/rGO). As can be observed in Figure 4a, the ternary nanocomposite demonstrates an improved absorption spectrum compared to the V_2O_5 nanoparticle, which confirms the better photocatalytic activity of V_2O_5−Fe_3O_4/rGO. The absorption spectra of both nanostructures indicate absorption in the UV region enlarging to the visible region, and this can be taken into account as a consequence of the transformation of charges from the valence band of O 2p to the vacant orbitals of V 3d in the conduction band.[69,70] Figure 4b,c displays the Tauc plots of V_2O_5 and the V_2O_5−Fe_3O_4/rGO nanocomposite, and their optical band gaps are determined by using Tauc's equation (eq 2):

$$\alpha h\nu = \mathrm{A}(h\nu - E_g)^{n/2} \tag{2}$$

In the above equation, α is the absorption coefficient, h is Planck's constant, and ν and E_g are the light frequency and band gap energy, respectively. In the case of nondirect transition in semiconductors, the value assigned to n is 1, while for a direct transition, the value is set to 4. Figure 4b,c shows the obtained band gap energies which are 1.86 and 2.16 eV for V_2O_5−Fe_3O_4/rGO and V_2O_5, respectively. UV−visible DRS results reveal the higher absorption edge of the ternary nanocomposite that results in lower band gap energy and better photocatalytic behavior in comparison with V_2O_5 nanoparticles.[71]

Moreover, the 705.8 cm^2/g total surface area of the ternary V_2O_5−Fe_3O_4/rGO nanocomposite is measured by N_2 adsorption−desorption data based on the type IV isotherm, as shown in Figure 5a. In addition, the BJH method was executed to calculate the nanocomposite's pore volume size, which was 0.065 cm^3/g, as well as the pore size of 46.13 nm.

Figure 5b displays the optical properties of V_2O_5 and V_2O_5−Fe_3O_4/rGO nanostructures, which are precisely determined by the PL technique. The results are beneficial for investigating the electron−hole pair recombination and their separation capacity in both types of nanophotocatalysts. In general, the lower intensity of V_2O_5−Fe_3O_4/rGO PL spectra compared with V_2O_5 nanoparticles results in a lower electron−hole pair recombination, and it illustrates enhanced separation capacity. In addition, the substantial emission bands at 485 and 543 nm are related to the recombination of the electrons and holes from the conduction band of V 3d to the valence band of O 2p.[72,73]

3.2. Photocatalytic Degradation Activity. Under direct UV and visible light irradiation, the photocatalytic activity of the synthesized ternary V_2O_5−Fe_3O_4/rGO nanocomposite on MB dye degradation was investigated at room temperature for 100 and 110 min, respectively, as can be observed in Figure 6a,b. The correlation between light absorption and factors such as the molar absorptivity, the length of the light trajectory, and the solution concentration can be described through the application of the Beer−Lambert law ($A = \varepsilon bC$).[74]

Where the decreasing trend of A indicates a decreasing trend in MB dye concentration, it also demonstrates the MB dye concentration in various time intervals in a degradation test. The maximum wavelength of MB dye was determined to be 664 nm by the use of UV−visible spectroscopy, and a control experiment was carried out to establish the adsorption−desorption equilibrium of MB dye. The obtained result displays the adsorption process and the ratio of V_2O_5−Fe_3O_4/rGO nanocomposites' absorbance reduction after 30

https://doi.org/10.1021/acsomega.3c06094
ACS Omega 2023, 8, 35427−35439

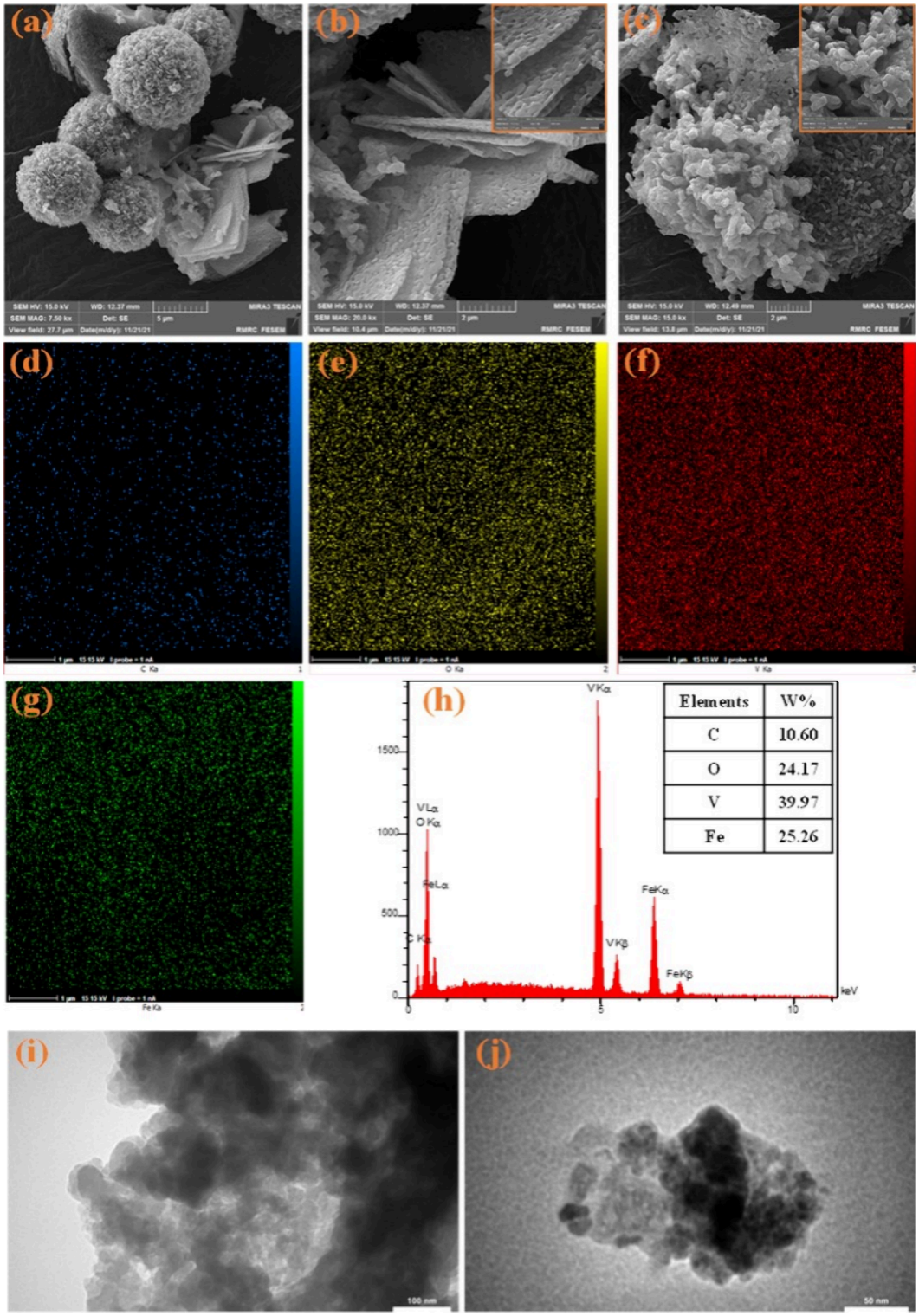

Figure 3. Images of (a−c) FE-SEM, elemental mapping of (d) C, (e) O, (f) V, and (g) Fe elements, (h) EDS analysis, and (i, j) TEM of ternary V_2O_5−Fe_3O_4/rGO nanocomposite. The insets in (b) and (c) show a magnified image of two various morphologies of the the V_2O_5−Fe_3O_4/rGO nanocomposite. The inset table in (h) indicates the elemental weight percentages obtained from the EDS results.

min in a dark situation. The absorbance reduction continued for 100 and 110 min under UV and visible-light irradiation after achieving adsorption−desorption equilibrium to present 89.2 and 76% photocatalytic degradation, respectively. The pseudo-first-order kinetic model was employed to investigate the kinetics of MB degradation under two distinct irradiation sources, UV and visible radiation. The following equation (eq 3) is widely used to calculate the rate of degradation over time using this model:

$$-\ln(A_t/A) = k_{obs} \cdot t \quad (3)$$

As can be seen in the insets of Figure 6a,b, the higher measured reaction rate value (k_{obs}) indicates a faster response

https://doi.org/10.1021/acsomega.3c06094
ACS Omega 2023, 8, 35427−35439

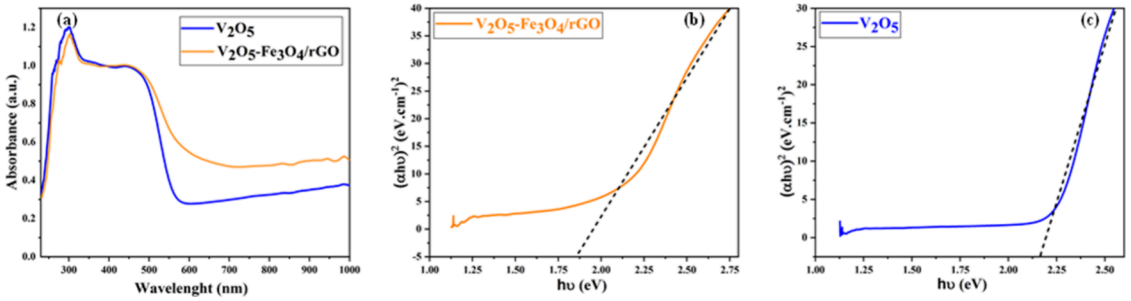

Figure 4. (a) UV−visible diffuse reflectance spectra of V_2O_5 and V_2O_5−Fe_3O_4/rGO; optical band gap plot of (b) ternary V_2O_5−Fe_3O_4/rGO nanocomposite and (c) V_2O_5 nanoparticles.

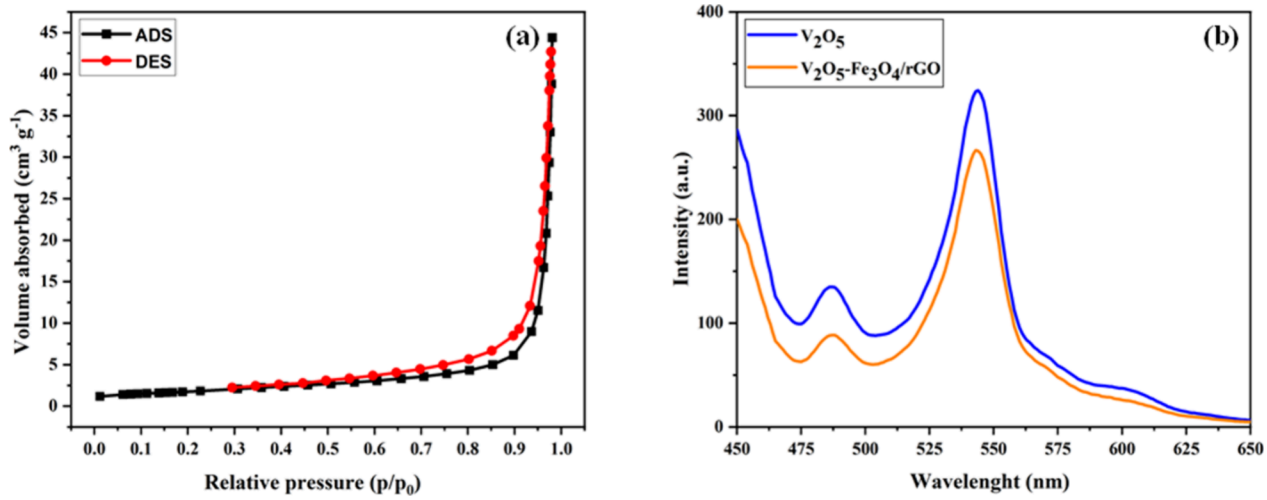

Figure 5. (a) N_2 adsorption−desorption data of the V_2O_5−Fe_3O_4/rGO nanocomposite. (b) Photoluminescence spectra of V_2O_5 and V_2O_5−Fe_3O_4/rGO samples.

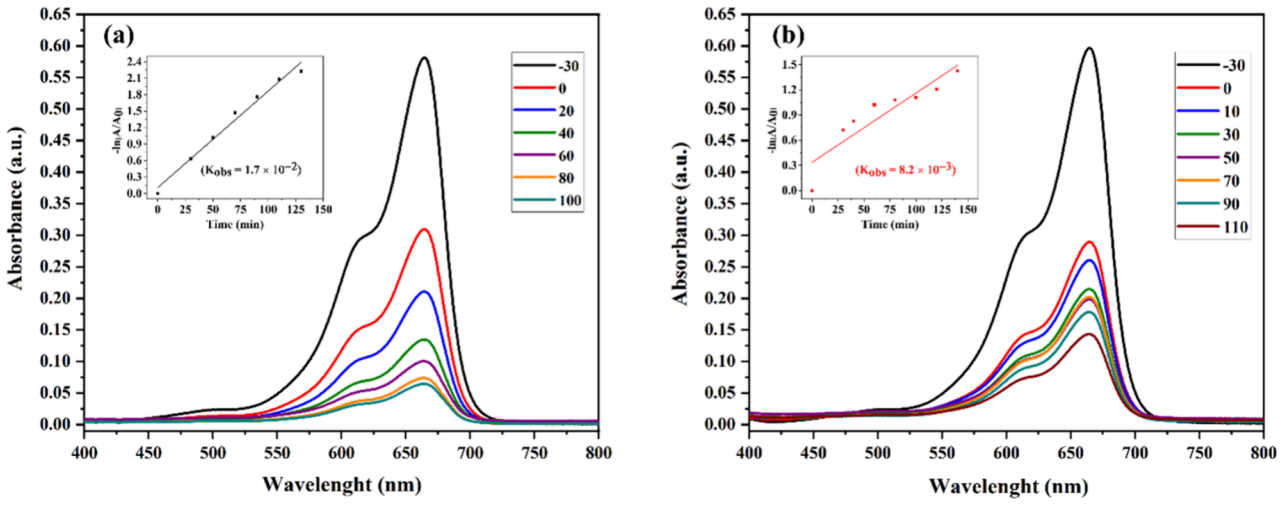

Figure 6. UV−visible spectra of MB dye solution in the presence of the V_2O_5−Fe_3O_4/rGO photocatalyst (a) under UV light (b) and visible light, respectively. The insets show the $-\ln[A/A_0]$ vs time (min) plot of V_2O_5−Fe_3O_4/rGO (a) under UV light irradiation and (b) visible-light irradiation, respectively.

to photocatalytic degradation, which is related to performing a photocatalytic process under UV irradiation.

Further, comparative experiments were conducted to determine the photocatalytic degradation of MB dye under UV light irradiation at room temperature and in the neutral pH for all the synthesized samples including GO substrate, V_2O_5 and Fe_3O_4 nanoparticles, binary Fe_3O_4@rGO and V_2O_5@rGO nanocomposites, and ternary V_2O_5−Fe_3O_4/rGO nanocomposite (and also under dark condition), as shown in Figure 7a. It can be seen that V_2O_5 nanoparticles and V_2O_5@rGO nanocomposites indicate higher degradation efficiencies of MB dye compared to both Fe_3O_4 nanoparticles and Fe_3O_4@rGO; therefore, V_2O_5 and V_2O_5@rGO nanostructures play a more vital role in the degradation mechanism of MB dye. The

https://doi.org/10.1021/acsomega.3c06094
ACS Omega 2023, 8, 35427−35439

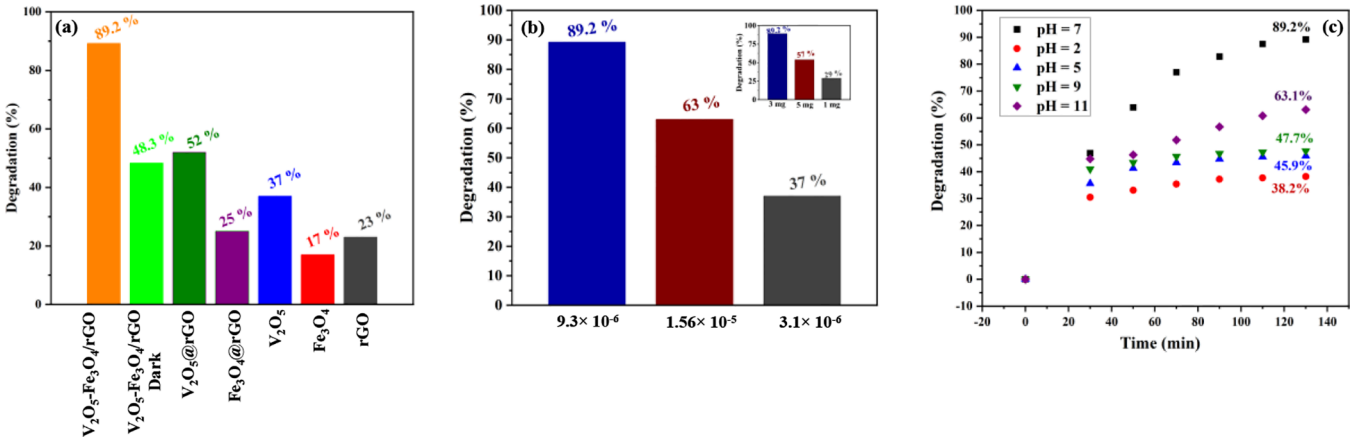

Figure 7. (a) Comparative photodegradation efficiency of MB dye using synthesized samples including rGO, V_2O_5, Fe_3O_4, V_2O_5@rGO, and Fe_3O_4@rGO, and V_2O_5−Fe_3O_4/rGO nanocomposites under both dark and UV light conditions. (b) Comparative MB dye degradation percentages for different dye concentrations; the inset displays the degradation efficiency of MB for different dosages of the ternary photocatalyst. (c) Photocatalytic degradation of MB dye at different pH values.

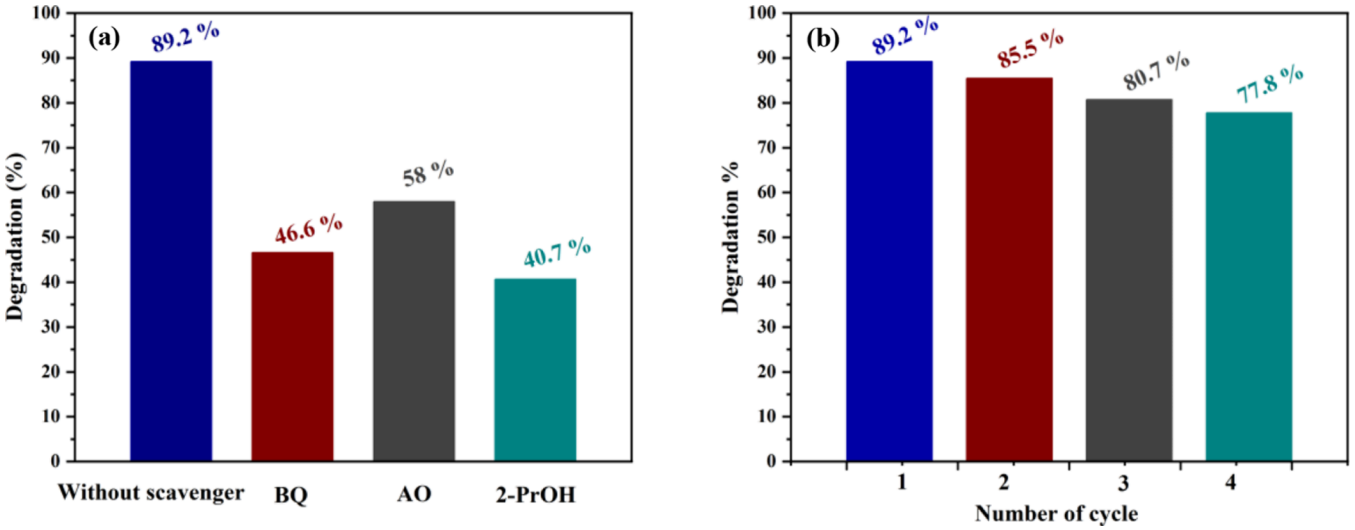

Figure 8. (a) Photodegradation efficiency of MB dye in the presence of BQ, AO, and 2-PrOH as quenchers and (b) reusability and percentages of MB degradation by V_2O_5−Fe_3O_4/rGO for four continued cycles.

degradation efficiency has been raised by using rGO as an electron acceptor in V_2O_5@rGO and Fe_3O_4@rGO binary nanocomposites in comparison to the photocatalytic degradation of V_2O_5 and Fe_3O_4 nanoparticles. Furthermore, the degradation percentage under dark situation shows the adsorption capacity of the ternary nanocomposite due to the absence of light irradiation and degradation process. The synergistic effect in the V_2O_5−Fe_3O_4/rGO nanocomposite and the reservoir of photogenerated electrons in the rGO surface resulted in a higher degradation ratio compared to all the synthesized nanostructures, which can be seen in Figure 7a. Totally, by using the rGO support, a higher degradation efficiency can be achieved due to the less electron−hole pair recombination, lower band gap energy, and higher charge separation, which are consistent with DRS and PL results.

To achieve the best photocatalytic performance and efficiency, we optimize the dosage of the photocatalyst, dye concentration, and pH media. The inset of Figure 7b presents the use of three various dosages including 1, 3, and 5 mg of the V_2O_5−Fe_3O_4/rGO nanocomposite and also the obtained results based on the different concentrations (e.g., 3.1 × 10^{-6}, 9.38 × 10^{-6}, and 1.56 × 10^{-5} M) of MB dye shown in Figure 7b. Actually, the highest ratio of adsorbent mass to adsorbate concentration is related to 3 mg of photocatalyst loading mass in the presence of 9.38 × 10^{-6} M dye solution. The reduction in the accessibility of active sites on the photocatalyst surface is correlated with a rise in the concentration of the dye. As the catalyst mass increases, the surface area available for the dye molecule also increases, resulting in an enhanced interaction between the dye molecule and the catalyst. However, an excessive increase in the concentration of the photocatalyst leads to the aggregation of nanoparticles, causing a reduction in the number of active surface sites to absorb light. In addition, to consider the pH effect on the photocatalytic degradation process, a wide range of pH was used, and the results are plotted in Figure 7c. The degradation efficiency of the V_2O_5−Fe_3O_4/rGO nanocomposite in various acidic and basic media, e.g., pH = 2, 5, 9, and 11, was found to be 38.2, 45.9, 47.7, and 63.1%, respectively. Among all used pH, the highest degradation efficiency using the ternary nanophotocatalyst is related to the neutral pH with 89.2% degradation of MB dye. In an alkaline solution, the

https://doi.org/10.1021/acsomega.3c06094
ACS Omega 2023, 8, 35427−35439

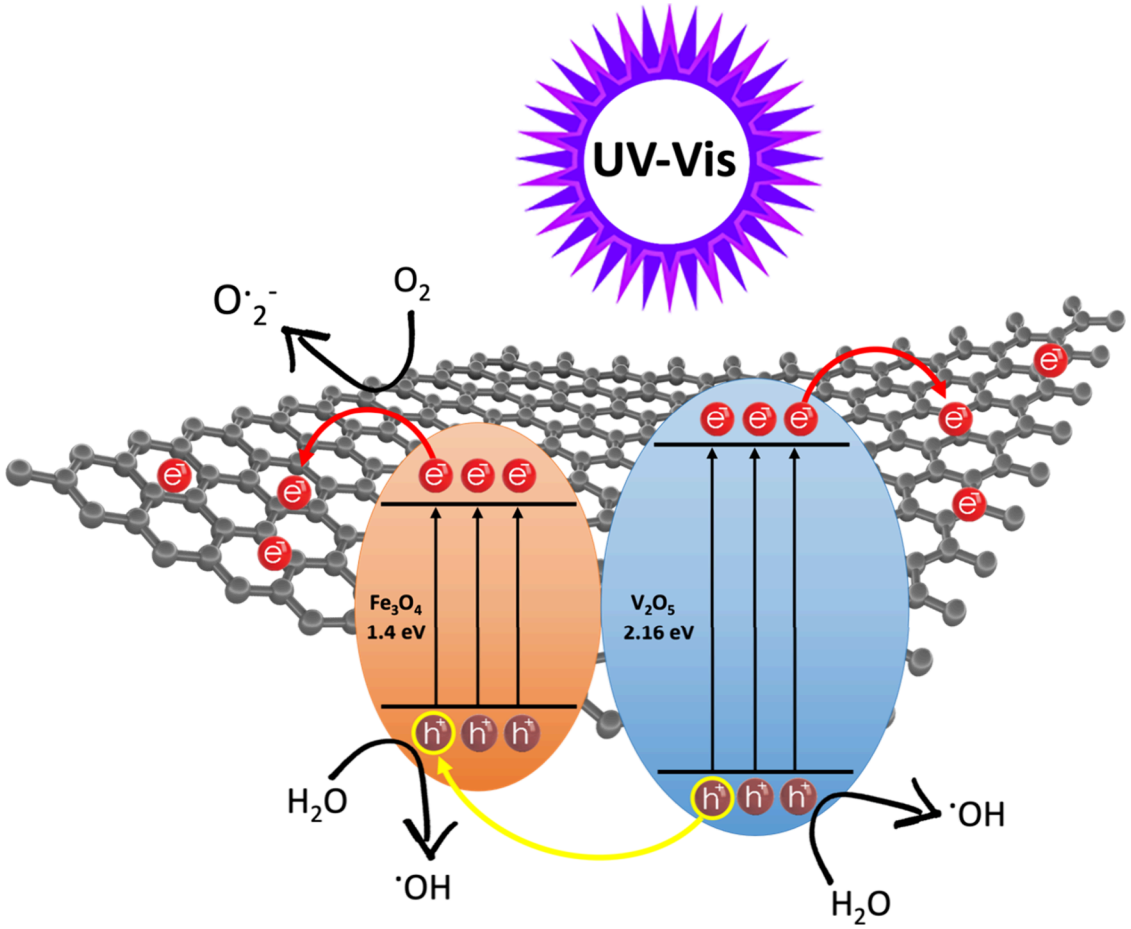

Figure 9. Schematic of the possible photocatalytic activity of the V_2O_5−Fe_3O_4/rGO nanocomposite for MB photodegradation.

abundance of hydroxyl ions can lead to the generation of hydroxyl radicals, which may be a contributing factor to the improved photocatalytic degradation of MB at higher pH conditions.

Furthermore, to investigate the degradation mechanism of the V_2O_5−Fe_3O_4/rGO nanocomposite, quenching studies have been employed to determine the functions of reactive oxygen species, as seen in Figure 8a. For this purpose, 0.1 mM benzoquinone (BQ), 2-propanol (2-PrOH,), and ammonium oxalate (AO), as $O_2^{\cdot-}$, $OH^{\cdot}$, and H^+ scavengers, respectively, were utilized to illustrate the most significant factor in the photocatalytic degradation of MB dye. In the existence of BQ, 2-PrOH, and AO, the degradation efficiency reduced from 89.2 to 46.6, 40.7, and 58%, respectively. Quenching experiments showed the crucial role of $O_2^{\cdot-}$and $OH^{\cdot}$ species in the degradation tests. As can be observed in Figure 9, exposing V_2O_5 and Fe_3O_4 semiconductors to direct UV/visible light results in electron transfer from the valence band to the conduction band, creating h^+ in the valence band (eq 4). As mentioned above, the role of 2D rGO nanosheets is so crucial for less electron−hole pair recombination of the ternary nanocomposite due to the surface vacant active sites of rGO nanosheets compared to the poor degradation efficiency of non-rGO-based nanostructures. Electrons that have been stimulated by light on the rGO nanosheets can engage in reaction with the dissolved O_2, causing the formation of $O_2^{\cdot-}$, as well as react with the functional groups that remain on rGO, which leads to a rise in oxide radicals (eqs 5−7). In the valence bands of both V_2O_5 and Fe_3O_4, h^+ can react with H_2O molecules, which results in the generation of $OH^{\cdot}$ and improving MB dye degradation in the solution; also, h^+ can be transferred to the valence band of Fe_3O_4 from the valence band of V_2O_5, due to the lower band gap energy of Fe_3O_4 (eq 8).[39,75] The $OH^{\cdot}$ and $O_2^{\cdot-}$ radicals are quite active and are the main reasons for MB dye degradation under irradiation, consistent with the quenching experiment results (eq 9).

$$V_2O_5 - Fe_3O_4/rGO + h\nu \rightarrow V_2O_5 - Fe_3O_4/rGO(h^+_{VB} + e^-_{CB}) \quad (4)$$

$$V_2O_5 - Fe_3O_4/rGO(e^-_{CB}) + O_2 \rightarrow V_2O_5 - Fe_3O_4/rGO + O_2^{\cdot-} \quad (5)$$

$$rGO(e^-) + O_2 \rightarrow rGO + O_2^{\cdot-} \quad (6)$$

$$rGO(e^-) + O_2^{\cdot-} + H_2O \rightarrow HO_2^{\cdot} + OH^- \quad (7)$$

$$V_2O_5 - Fe_3O_4/rGO(h^+_{VB}) + OH^-/H_2O \rightarrow V_2O_5 - Fe_3O_4/rGO + OH^{\cdot} \quad (8)$$

$$MB + OH^{\cdot} + O_2^{\cdot-} \rightarrow CO_2 + H_2O \quad (9)$$

Furthermore, the nanocomposite's recyclability and reusability are crucial factors in the degradation process. The nanocomposite's recyclability was investigated to determine its long-term viability and presented in Figure 8b. The photocatalyst did not show a substantial loss of activity after four

https://doi.org/10.1021/acsomega.3c06094
ACS Omega 2023, 8, 35427−35439

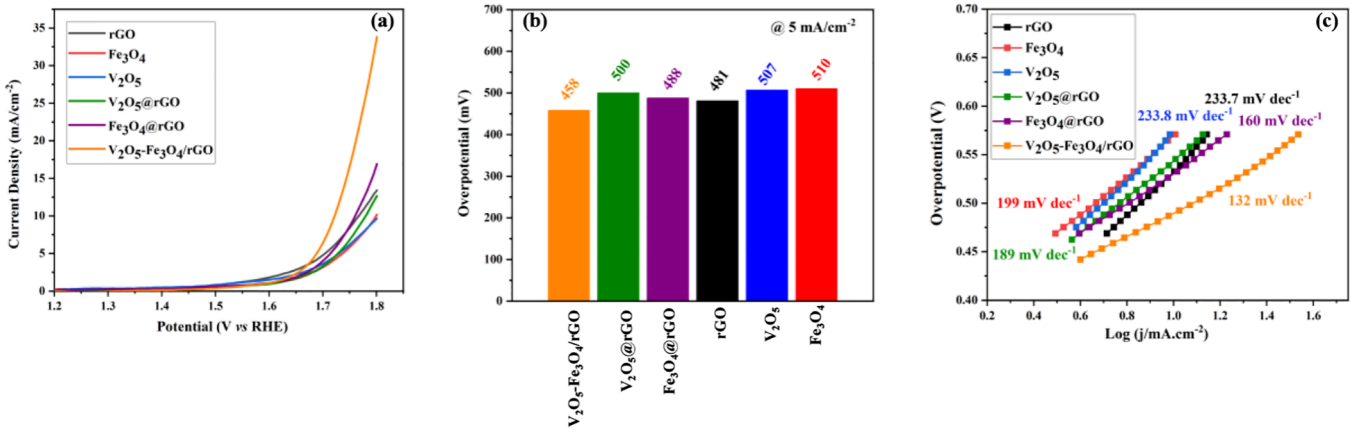

Figure 10. (a) OER polarization curves, (b) comparative overpotential (mV) at a current density of 5 mA/cm^{-2}, and (c) Tafel plots of rGO, Fe_3O_4, V_2O_5, V_2O_5@rGO, Fe_3O_4@rGO, and V_2O_5−Fe_3O_4/rGO in 1 M KOH.

cycles of degradation, and it can be utilized repeatedly. After four cycles of degradation, the efficiency was reduced by roughly 11.4% to achieve 77.8% MB degradation, indicating that the novel synthesized ternary V_2O_5−Fe_3O_4/rGO photocatalyst is stable throughout the photocatalytic degradation.

3.3. Electrocatalytic Activity of Synthesized Samples.

To investigate the secondary application of the above-mentioned synthesized nanostructures, an electrochemical measurement was conducted to obtain the best electrocatalytic performance for the OER. In Figure 10a, the polarization curves by linear sweep voltammetry are demonstrated, and they show the OER activities of the nanostructures. As displayed in Figure 10b, the overpotential of V_2O_5−Fe_3O_4/rGO (458 mV) is significantly lower than that of rGO (481 mV), Fe_3O_4@rGO (488 mV), V_2O_5@rGO (500 mV), V_2O_5 (507 mV), and Fe_3O_4 (510 mV), which confirms the positive role of the synergistic effect on electrocatalytic oxygen evolution. Meanwhile, the lowest Tafel slope is depicted for V_2O_5−Fe_3O_4/rGO, which is 132 mV dec^{-1}, compared to Fe_3O_4@rGO (160 mV dec^{-1}), V_2O_5@rGO (189 mV dec^{-1}), Fe_3O_4 (199 mV dec^{-1}), rGO (233.7 mV dec^{-1}), and V_2O_5 (233.8 mV dec^{-1}) in Figure 10c. The acquired results indicate that rGO nanosheets can remarkably improve the electrocatalytic oxygen evolution performance of nanoparticles, and the primary reason is highly associated with the surface-active sites of the 2D structure of rGO nanosheets in both binary and ternary nanocomposites. Moreover, in the ternary nanocomposite, V_2O_5 nanoparticles can serve as active sites, and Fe_3O_4 nanoparticle can oxidize water which results in better performance for OER. A possible mechanism is the absorption of OH^- by the V_2O_5−Fe_3O_4/rGO nanocomposite on the rGO and V_2O_5 active sites, which leads to the formation of the OOH* species. On the other hand, water is oxidized by Fe_3O_4 to generate O_2^- and H^+ ions; therefore, O_2^- species combine with OOH* species to form O_2 molecules, which are released into the gas phase.[57] In conjunction with the results of the OER, EIS analyses were performed for further investigations of the electrochemical behavior of the V_2O_5−Fe_3O_4/rGO nanocomposite. As shown in Figure S4 (Supporting Information), the smallest charge-transfer resistance is displayed for the ternary nanocatalyst compared to V_2O_5@rGO and Fe_3O_4@rGO, which is attributed to the developed kinetic reactions in the V_2O_5−Fe_3O_4/rGO nanocomposite.

4. CONCLUSIONS

The dual applications of the ternary magnetic V_2O_5−Fe_3O_4/rGO nanocomposite in the photocatalytic degradation of MB dye and electrocatalytic oxygen evolution were investigated in this research compared to rGO, Fe_3O_4, V_2O_5, Fe_3O_4@rGO, and V_2O_5@rGO for the first time. Photocatalytic degradation of all the synthesized nanostructures revealed a higher efficiency of MB dye degradation by the ternary nanocomposite due to the synergistic effect of both V_2O_5 and Fe_3O_4 semiconductors modified on the rGO nanosheets. The obtained results of the ternary nanocomposite reveal that 89.2 and 76% degradation occurred in neutral pH at room temperature under UV and visible-light irradiation, respectively. Also, the magnetic property of V_2O_5−Fe_3O_4/rGO was very practical for four rounds of recycling and easy separation of the catalyst after degradation tests. Moreover, based on the PL and DRS results, the presence of both V_2O_5 and Fe_3O_4 nanoparticles on the rGO nanosheets in V_2O_5−Fe_3O_4/rGO can remarkably reduce the intensity and the optical band gap energy, which results in better charge transfer and lower electron−hole pair recombination. Furthermore, the highest performance of oxygen evolution activity with the overpotential of 458 mV and Tafel slope of 132 mV dec^{-1} was obtained with V_2O_5−Fe_3O_4/rGO in the LSV test compared to rGO, Fe_3O_4, V_2O_5, Fe_3O_4@rGO, and V_2O_5@rGO. The 2D structure of rGO nanosheets can help them function as electron acceptors, and it is beneficial for better charge separation in both photocatalytic and electrocatalytic applications. Also, due to the reactive sites of V_2O_5 nanoparticles and the high electrical conductivity of Fe_3O_4 nanoparticles, they both can significantly increase the electrocatalytic behavior of the ternary nanocatalyst for OER.

■ ASSOCIATED CONTENT

Supporting Information

The Supporting Information is available free of charge at https://pubs.acs.org/doi/10.1021/acsomega.3c06094.

Elemental mapping and EDS analysis of binary nanocomposites, Raman spectrum of V_2O_5−Fe_3O_4/rGO, and EIS analyses of nanocomposites (PDF)

https://doi.org/10.1021/acsomega.3c06094
ACS Omega 2023, 8, 35427−35439

AUTHOR INFORMATION

Corresponding Author

Fatemeh Rahnemaye Rahsepar − *School of Chemistry, College of Science, University of Tehran, Tehran 1417614411, Iran;* orcid.org/0000-0003-2359-2523; Email: frahsepar@ut.ac.ir

Author

Fatemeh Jafari − *School of Chemistry, College of Science, University of Tehran, Tehran 1417614411, Iran*

Complete contact information is available at: https://pubs.acs.org/10.1021/acsomega.3c06094

Author Contributions

The manuscript was written through contributions of all authors. All authors have given approval to the final version of the manuscript.

Notes

The authors declare no competing financial interest.

REFERENCES

(1) Yan, Y.; Shin, W. I.; Chen, H.; Lee, S.-M.; Manickam, S.; Hanson, S.; Zhao, H.; Lester, E.; Wu, T.; Pang, C. H. A recent trend: application of graphene in catalysis. *Carbon Lett.* **2021**, *31*, 177−199.

(2) Qian, W.; Xu, S.; Zhang, X.; Li, C.; Yang, W.; Bowen, C. R.; Yang, Y. Differences and Similarities of Photocatalysis and Electrocatalysis in Two-Dimensional Nanomaterials: Strategies, Traps, Applications and Challenges. *Nanomicro Lett.* **2021**, *13* (1), 156.

(3) Punia, P.; Bharti, M.; Chalia, S.; Dhar, R.; Ravelo, B.; Thakur, P.; Thakur, A. Recent advances in synthesis, characterization, and applications of nanoparticles for contaminated water treatment- A review. *Ceram. Int.* **2021**, *47*, 1526−1550.

(4) Thongam, D. D.; Chaturvedi, H. Advances in nanomaterials for heterogeneous photocatalysis. *Nano Express* **2021**, *2* (1), No. 012005.

(5) Pang, Y. L.; Lim, S.; Ong, H. C.; Chong, W. T. Research progress on iron oxide-based magnetic materials: synthesis techniques and photocatalytic applications. *Ceram. Int.* **2016**, *42* (1), 9−34.

(6) Koe, W. S.; Lee, J. W.; Chong, W. C.; Pang, Y. L.; Sim, L. C. An overview of photocatalytic degradation: photocatalysts, mechanisms, and development of photocatalytic membrane. *Environ. Sci. Pollut. Res.* **2020**, *27*, 2522−2565.

(7) Bhatkhande, D. S.; Pangarkar, V. G.; Beenackers, A. A. C. M. Photocatalytic degradation for environmental applications−a review. *J. Chem. Technol. Biotechnol.* **2002**, *77* (1), 102−116.

(8) Julkapli, N. M.; Bagheri, S. Graphene supported heterogeneous catalysts: An overview. *Int. J. Hydrogen Energy* **2015**, *40* (2), 948−979.

(9) Yam, K. M.; Guo, N.; Jiang, Z.; Li, S.; Zhang, C. Graphene-based heterogeneous catalysis: Role of graphene. *Catalysts* **2020**, *10* (1), 53.

(10) Singh, V.; Joung, D.; Zhai, L.; Das, S.; Khondaker, S. I.; Seal, S. Graphene based materials: past, present and future. *Prog. Mater. Sci.* **2011**, *56* (8), 1178−1271.

(11) Bolotin, K. I.; Sikes, K.; Jiang, Z.; Klima, M.; Fudenberg, G.; Hone, J.; Kim, P.; Stormer, H. L. Ultrahigh electron mobility in suspended graphene. *Solid State Commun.* **2008**, *146* (9−10), 351−355.

(12) Huang, X.; Yin, Z.; Wu, S.; Qi, X.; He, Q.; Zhang, Q.; Yan, Q.; Boey, F.; Zhang, H. Graphene-based materials: synthesis, characterization, properties, and applications. *Small* **2011**, *7* (14), 1876−1902.

(13) Balandin, A. A.; Ghosh, S.; Bao, W.; Calizo, I.; Teweldebrhan, D.; Miao, F.; Lau, C. N. Superior thermal conductivity of single-layer graphene. *Nano Lett.* **2008**, *8* (3), 902−907.

(14) Basu, S.; Bhattacharyya, P. Recent developments on graphene and graphene oxide based solid state gas sensors. *Sens. Actuators, B* **2012**, *173*, 1−21.

(15) Duan, Z. *Application of graphene in metal corrosion protection*. In IOP Conference Series: Materials Science and Engineering; IOP Publishing: 2019.

(16) Kim, J.; Cote, L. J.; Kim, F.; Yuan, W.; Shull, K. R.; Huang, J. Graphene oxide sheets at interfaces. *J. Am. Chem. Soc.* **2010**, *132* (23), 8180−8186.

(17) Jamjoum, H. A. A.; Umar, K.; Adnan, R.; Razali, M. R.; Mohamad Ibrahim, M. N. Synthesis, characterization, and photocatalytic activities of graphene oxide/metal oxides nanocomposites: A review. *Front. Chem.* **2021**, *9*, No. 752276.

(18) Jenifer, A.; Sastri, M. S.; Sriram, S. Photocatalytic dye degradation of V_2O_5 Nanoparticles—An experimental and DFT analysis. *Optik* **2021**, *243*, No. 167148.

(19) Sajid, M. M.; Shad, N. A.; Javed, Y.; Khan, S. B.; Zhang, Z.; Amin, N.; Zhai, H. Preparation and characterization of Vanadium pentoxide (V_2O_5) for photocatalytic degradation of monoazo and diazo dyes. *Surf. Interfaces* **2020**, *19*, No. 100502.

(20) Celestino-Santos, W.; Bezerra, A., Jr; Cezar, A.; Mattoso, N.; Schreiner, W. Vanadium oxide nanoparticles as optical sensors of cysteine. *J. Nanosci. Nanotechnol.* **2011**, *11* (6), 4702−4707.

(21) Le, T. K.; Kang, M.; Kim, S. W. Relation of photoluminescence and sunlight photocatalytic activities of pure V_2O_5 nanohollows and V_2O_5/RGO nanocomposites. *Mater. Sci. Semicond. Process.* **2019**, *100*, 159−166.

(22) Ashery, M. H.; Elnouby, M.; EL-Maghraby, E.; Elsehly, E. Structural control of V_2O_5 nanoparticles via a thermal decomposition method for prospective photocatalytic applications. *Beni-Suef Univ. J. Basic Appl. Sci.* **2023**, *12* (1), 12.

(23) Kruefu, V.; Sintuya, H.; Pookmanee, P.; Phanichphant, S. *Visible light photocatalytic degradation of methylene blue using V_2O_5nanoparticles*. In 6th International Conference on Developments in Engineering and Technology (ICDET-2017), 2017.

(24) Aliaga, J.; Cifuentes, N.; González, G.; Sotomayor-Torres, C.; Benavente, E. Enhancement photocatalytic activity of the heterojunction of two-dimensional hybrid semiconductors ZnO/V_2O_5. *Catalysts* **2018**, *8* (9), 374.

(25) Su, J.; Zou, X.-X.; Li, G.-D.; Wei, X.; Yan, C.; Wang, Y.-N.; Zhao, J.; Zhou, L.-J.; Chen, J.-S. Macroporous V_2O_5− $BiVO_4$ composites: effect of heterojunction on the behavior of photogenerated charges. *J. Phys. Chem. C* **2011**, *115* (16), 8064−8071.

(26) Bhardwaj, D.; Sangwan, S.; Shivashankar, S.; Umarji, A. M. Microwave-assisted synthesis of reduced graphene oxide/V_2O_5 nanocomposite as an efficient photocatalyst for dye degradation. *Bull. Mater. Sci.* **2022**, *45* (3), 135.

(27) Kumar, B.; Smita, K.; Cumbal, L.; Debut, A.; Galeas, S.; Guerrero, V. H. Phytosynthesis and photocatalytic activity of magnetite (Fe_3O_4) nanoparticles using the Andean blackberry leaf. *Mater. Chem. Phys.* **2016**, *179*, 310−315.

(28) Wang, B.-Y.; Huang, S.-Y.; Hsiao, Y.-S.; Wei, P.-C.; Chou, C.-M.; Hsiao, V. K. Pulsed-Laser Induced Photolysis of Synthesizing Magnetic Fe_3O_4 Nanoparticles for Visible-Light Photocatalysis. *Catalysts* **2022**, *12* (11), 1459.

(29) Padhi, D. K.; Panigrahi, T. K.; Parida, K.; Singh, S.; Mishra, d. P. Green synthesis of Fe_3O_4/RGO nanocomposite with enhanced photocatalytic performance for Cr (VI) reduction, phenol degradation, and antibacterial activity. *ACS Sustainable Chem. Eng.* **2017**, *5* (11), 10551−10562.

(30) Kumar, A. P.; Bilehal, D.; Desalegn, T.; Kumar, S.; Ahmed, F.; Murthy, H. A.; Kumar, D.; Gupta, G.; Chellappan, D. K.; Singh, S. K. Studies on synthesis and characterization of Fe_3O_4@SiO_2@Ru hybrid magnetic composites for reusable photocatalytic application. *Adsorp. Sci. Technol.* **2022**, *2022*, 1−18.

(31) Mirzaei, H.; Ehsani, M. H.; Shakeri, A.; Ganjali, M. R.; Badiei, A. Preparation and Photocatalytic application of Ternary Fe_3O_4/GQD/gC_3N_4 Heterostructure Photocatalyst for RhB Degradation. *Pollution (2383451X)* **2022**, *8* (3), 779−791.

(32) Mu, D.; Chen, Z.; Shi, H.; Tan, N. Construction of flower-like MoS_2/Fe_3O_4/rGO composite with enhanced photo-Fenton like catalyst performance. *RSC Adv.* **2018**, *8* (64), 36625−36631.

(33) Pudukudy, M.; Jia, Q.; Dong, Y.; Yue, Z.; Shan, S. Magnetically separable and reusable rGO/Fe_3O_4 nanocomposites for the selective liquid phase oxidation of cyclohexene to 1, 2-cyclohexane diol. *RSC Adv.* **2019**, *9* (56), 32517−32534.
(34) Vinothkannan, M.; Karthikeyan, C.; Kim, A. R.; Yoo, D. J. One-pot green synthesis of reduced graphene oxide (RGO)/Fe_3O_4 nanocomposites and its catalytic activity toward methylene blue dye degradation. *Spectrochim. Acta A: Mol. Biomol. Spectrosc.* **2015**, *136*, 256−264.
(35) Khan, M. M.; Khan, W.; Ahamed, M.; Alhazaa, A. N. Investigation on the structure and physical properties of Fe_3O_4/RGO nanocomposites and their photocatalytic application. *Mater. Sci. Semicond. Process.* **2019**, *99*, 44−53.
(36) Chaudhary, H.; Chaudhary, K.; Zulfiqar, S.; Saif, M. S.; Alsafari, I. A.; Shakir, I.; Agboola, P. O.; Safdar, M.; Warsi, M. F. Fabrication of reduced Graphene Oxide supported Gd3+ doped V_2O_5 nanorod arrays for superior photocatalytic and antibacterial activities. *Ceram. Int.* **2021**, *47* (23), 32521−32533.
(37) Yadav, A. A.; Hunge, Y. M.; Kang, S.-W.; Fujishima, A.; Terashima, C. Enhanced photocatalytic degradation activity using the V_2O_5/RGO composite. *Nanomaterials* **2023**, *13* (2), 338.
(38) Sharma, D.; Faraz, M.; Kumar, D.; Takhar, D.; Birajdar, B.; Khare, N. Visible light activated V_2O_5/rGO nanocomposite for enhanced photodegradation of methylene blue dye and photoelectrochemical water splitting. *Inorg. Chem. Commun.* **2022**, *142*, No. 109657.
(39) Boruah, P. K.; Szunerits, S.; Boukherroub, R.; Das, M. R. Magnetic Fe_3O_4@V_2O_5/rGO nanocomposite as a recyclable photocatalyst for dye molecules degradation under direct sunlight irradiation. *Chemosphere* **2018**, *191*, 503−513.
(40) Kanazawa, T.; Maeda, K.Photochemical synthesis of nanoscale multicomponent metal species and their application to photocatalytic and electrochemical water splitting. In *Nanostructured photocatalysts*; Elsevier: 2020; pp. 19−38. DOI: 10.3390/ijerph20126176.
(41) Mohsin, M.; Ishaq, T.; Bhatti, I. A.; Jilani, A.; Melaibari, A. A.; Abu-Hamdeh, N. H. Semiconductor Nanomaterial Photocatalysts for Water-Splitting Hydrogen Production: The Holy Grail of Converting Solar Energy to Fuel. *Nanomaterials* **2023**, *13* (3), 546.
(42) Sapountzi, F. M.; Gracia, J. M.; Fredriksson, H. O.; Niemantsverdriet, J. H. Electrocatalysts for the generation of hydrogen, oxygen and synthesis gas. *Prog. Energy Combust. Sci.* **2017**, *58*, 1−35.
(43) Sardar, K.; Petrucco, E.; Hiley, C. I.; Sharman, J. D.; Wells, P. P.; Russell, A. E.; Kashtiban, R. J.; Sloan, J.; Walton, R. I. Water-splitting electrocatalysis in acid conditions using ruthenate-iridate pyrochlores. *Angew. Chem., Int. Ed. Engl.* **2014**, *53* (41), 10960−10964.
(44) Wang, S.; Lu, A.; Zhong, C.-J. Hydrogen production from water electrolysis: role of catalysts. *Nano Converg.* **2021**, *8* (1), 4.
(45) Choi, Y. H. VO2 as a Highly Efficient Electrocatalyst for the Oxygen Evolution Reaction. *Nanomaterials* **2022**, *12* (6), 939.
(46) Mounasamy, V.; Srividhya, G.; Ponpandian, N. Well-defined 2D transition vanadium pentoxide (V2O5) flat nanorods with large-scale synthesis feasibility as an electrocatalyst for the oxygen evolution reaction (OER). *Energy Adv.* **2023**, *2* (6), 784−788.
(47) Wei, M.; Han, Y.; Liu, Y.; Su, B.; Yang, H.; Lei, Z. Green preparation of Fe3O4 coral-like nanomaterials with outstanding magnetic and OER properties. *J. Alloys Compd.* **2020**, *831*, No. 154702.
(48) Bianchetti, E.; Perilli, D.; Di Valentin, C. Improving the Oxygen Evolution Reaction on Fe3O4 (001) with Single-Atom Catalysts. *ACS Catal.* **2023**, *13* (7), 4811−4823.
(49) Huang, W.; Peng, C.; Tang, J.; Diao, F.; Yesibolati, M. N.; Sun, H.; Engelbrekt, C.; Zhang, J.; Xiao, X.; Mølhave, K. S. Electronic structure modulation with ultrafine Fe3O4 nanoparticles on 2D Ni-based metal-organic framework layers for enhanced oxygen evolution reaction. *J. Energy Chem.* **2022**, *65*, 78−88.
(50) Luo, Y.; Yang, H.; Ma, P.; Luo, S.; Zhao, Z.; Ma, J. Fe3O4/CoO interfacial nanostructure supported on carbon nanotubes as a highly efficient electrocatalyst for Oxygen Evolution Reaction. *ACS Sustainable Chem. Eng.* **2020**, *8* (8), 3336−3346.
(51) Kaplan, B. Y.; Haghmoradi, N.; Biçer, E.; Merino, C.; Gürsel, S. A. High performance electrocatalysts supported on graphene based hybrids for polymer electrolyte membrane fuel cells. *Int. J. Hydrogen Energy* **2018**, *43* (52), 23221−23230.
(52) Quesnel, E.; Roux, F.; Emieux, F.; Faucherand, P.; Kymakis, E.; Volonakis, G.; Giustino, F.; Martín-García, B.; Moreels, I.; Gürsel, S. A. Graphene-based technologies for energy applications, challenges and perspectives. *2D Mater.* **2015**, *2* (3), No. 030204.
(53) Ali, A.; Shen, P. K. Recent progress in graphene-based nanostructured electrocatalysts for overall water splitting. *Electrochem. Energy Rev.* **2020**, *3*, 370−394.
(54) Shen, F.-C.; Wang, Y.; Tang, Y.-J.; Li, S.-L.; Wang, Y.-R.; Dong, L.-Z.; Li, Y.-F.; Xu, Y.; Lan, Y.-Q. CoV2O6−V2O5 coupled with porous N-doped reduced graphene oxide composite as a highly efficient electrocatalyst for oxygen evolution. *ACS Energy Lett.* **2017**, *2* (6), 1327−1333.
(55) Yang, J.; Zhu, G.; Liu, Y.; Xia, J.; Ji, Z.; Shen, X.; Wu, S. Fe3O4-decorated Co9S8 nanoparticles in situ grown on reduced graphene oxide: a new and efficient electrocatalyst for oxygen evolution reaction. *Adv. Funct. Mater.* **2016**, *26* (26), 4712−4721.
(56) Zaaba, N.; Foo, K.; Hashim, U.; Tan, S.; Liu, W.-W.; Voon, C. Synthesis of graphene oxide using modified hummers method: solvent influence. *Procedia Eng.* **2017**, *184*, 469−477.
(57) Liu, H.; Zhu, W.; Long, D.; Zhu, J.; Pezzotti, G. Porous V2O5 nanorods/reduced graphene oxide composites for high performance symmetric supercapacitors. *Appl. Surf. Sci.* **2019**, *478*, 383−392.
(58) Luo, J.; Jiang, D.; Liu, T.; Peng, J.; Chu, Z.; Jin, W. High-performance electrochemical mercury aptasensor based on synergistic amplification of Pt nanotube arrays and Fe3O4/rGO nanoprobes. *Biosens. Bioelectron.* **2018**, *104*, 1−7.
(59) Qilong, S.; Lei, S.; Yingying, C.; Wei, Y.; Sijun, X.; Tao, J.; Guoqiu, Y. Fe3O4-intercalated reduced graphene oxide nanocomposites with enhanced microwave absorption properties. *Ceram. Int.* **2019**, *45* (15), 18298−18305.
(60) Shanmugam, M.; Alsalme, A.; Alghamdi, A.; Jayavel, R. Enhanced photocatalytic performance of the graphene-V2O5 nanocomposite in the degradation of methylene blue dye under direct sunlight. *ACS Appl. Mater. Interfaces* **2015**, *7* (27), 14905−14911.
(61) Faniyi, I.; Fasakin, O.; Olofinjana, B.; Adekunle, A.; Oluwasusi, T.; Eleruja, M.; Ajayi, E. The comparative analyses of reduced graphene oxide (RGO) prepared via green, mild and chemical approaches. *SN Appl. Sci.* **2019**, *1*, 1181.
(62) Chen, D.; Yi, R.; Chen, S.; Xu, T.; Gordin, M. L.; Lv, D.; Wang, D. Solvothermal synthesis of V2O5/graphene nanocomposites for high performance lithium ion batteries. *Mater. Sci. Eng.: B* **2014**, *185*, 7−12.
(63) Jiang, X.; Li, L.; Cui, Y.; Cui, F. New branch on old tree: green-synthesized RGO/Fe3O4 composite as a photo-Fenton catalyst for rapid decomposition of methylene blue. *Ceram. Int.* **2017**, *43* (16), 14361−14368.
(64) Singh, N.; Kothari, D.; Ansari, J. R.; Pal, M.; Mandal, S.; Dhara, S.; Datta, A. Light-Induced Tunable n-Doping of Ag-Embedded GO/RGO Sheets in Polymer Matrix. *J. Phys. Chem. C* **2019**, *123* (16), 10557−10563.
(65) Yew, Y. P.; Shameli, K.; Miyake, M.; Khairudin, N. B. B. A.; Mohamad, S. E. B.; Hara, H.; Nordin, M. F. B. M.; Lee, K. X. An eco-friendly means of biosynthesis of superparamagnetic magnetite nanoparticles via marine polymer. *IEEE Trans. Nanotechnol.* **2017**, *16* (6), 1047−1052.
(66) Rosaiah, P.; Sandhya, G. L.; Hussain, O. Impedance spectroscopy and electrochemical properties of nano-crystalline vanadium pentoxide (V2O5) synthesized by co-precipitation method. *Adv. Sci. Eng. Med.* **2016**, *8* (2), 83−90.
(67) Munasir; Kusumawati, R. Synthesis and characterization of Fe3O4@ rGO composite with wet-mixing (ex-situ) process. *J. Phys.: Conf. Ser.* **2019**, *1171*, No. 012048, DOI: 10.1088/1742-6596/1171/1/012048.

(68) Mohan, H.; Selvaraj, D.; Kuppusamy, S.; Venkatachalam, J.; Park, Y. J.; Seralathan, K. K.; Oh, B. T. E-waste based V2O5/RGO/Pt nanocomposite for photocatalytic degradation of oxytetracycline. *Environ. Prog. Sustainable Energy* **2019**, *38* (4), 13123.
(69) Aawani, E.; Memarian, N.; Dizaji, H. R. Synthesis and characterization of reduced graphene oxide−V2O5 nanocomposite for enhanced photocatalytic activity under different types of irradiation. *J. Phys. Chem. Solids* **2019**, *125*, 8−15.
(70) Li, Y.; Kuang, J.-L.; Lu, Y.; Cao, W.-B. Facile synthesis, characterization of flower-like vanadium pentoxide powders and their photocatalytic behavior. *Acta Metallurg. Sinica* **2017**, *30*, 1017−1026.
(71) Shafique, S.; Yang, S.; Iqbal, T.; Cheng, B.; Wang, Y.; Sarwar, H.; Woldu, Y. T.; Ji, P. Improving the performance of V2O5/rGO hybrid nanocomposites for photodetector applications. *Sens. Actuators A: Phys.* **2021**, *332*, No. 113073.
(72) Thiagarajan, S.; Thaiyan, M.; Ganesan, R. Physical property exploration of highly oriented V2O5 thin films prepared by electron beam evaporation. *New J. Chem.* **2015**, *39* (12), 9471−9479.
(73) Pan, K.-Y.; Wei, D.-H. Optoelectronic and electrochemical properties of vanadium pentoxide nanowires synthesized by vapor-solid process. *Nanomaterials* **2016**, *6* (8), 140.
(74) Yulizar, Y.; Apriandanu, D. O. B.; Surya, R. M. Fabrication of novel SnWO4/ZnO using Muntingia calabura L. leaf extract with enhanced photocatalytic methylene blue degradation under visible light irradiation. *Ceram. Int.* **2022**, *48* (3), 3564−3577.
(75) Imran, M.; Alam, M. M.; Hussain, S.; Ali, M. A.; Shkir, M.; Mohammad, A.; Ahamad, T.; Kaushik, A.; Irshad, K. Highly photocatalytic active r-GO/Fe3O4 nanocomposites development for enhanced photocatalysis application: A facile low-cost preparation and characterization. *Ceram. Int.* **2021**, *47* (22), 31973−31982.

https://doi.org/10.1021/acsomega.3c06094
ACS Omega 2023, 8, 35427−35439